Photochemical & Photobiological Sciences (2022) 21:1201–1215
https://doi.org/10.1007/s43630-022-00209-z

ORIGINAL PAPERS

Ultrasonic-assisted decoration of Ag_2WO_4, AgI, and Ag nanoparticles over tubular g-C_3N_4: Plasmonic photocatalysts for impressive removal of tetracycline under visible light

Paria Hemmati-Eslamlu[1] · Aziz Habibi-Yangjeh[1] · Xuefei Xu[2] · Chundong Wang[2] · Alireza Khataee[3,4]

Received: 14 November 2021 / Accepted: 10 March 2022 / Published online: 5 April 2022

Abstract

The development of an efficient, eco-friendly, and low-cost photocatalyst is essential for addressing environmental and energy crises. In this regard, we report novel plasmonic photocatalysts through adorning tubular g-C_3N_4 with Ag_2WO_4, Ag, and AgI nanoparticles (TGCN/Ag/Ag_2WO_4/AgI) fabricated via a facile ultrasonic-irradiation procedure. The TGCN/Ag/Ag_2WO_4/AgI (20%) nanocomposite presented the excellent photocatalytic ability for removal of tetracycline hydrochloride under visible light, which was almost 45.6, 4.03, and 1.32 times more than GCN, TGCN, and TGCN/Ag/Ag_2WO_4 (20%) photocatalysts, respectively. Interestingly, the photocatalyst displayed impressive ability for the degradations of amoxicilline, rhodamine B, methyl orange, fuchsine, and methylene blue, which was 14.7, 52.2, 9.8, 13.2, and 7.46 times as much as pure GCN. The outcomes of DRS, PL, EIS, and photocurrent density analyses proved that the impressive activity could be related to the highly promoted harvesting of visible light, segregation of charge carriers, and improved charge migrations. In addition, trapping tests exhibited that $^{\bullet}O_2^-$ and h^+ were active species in the photocatalysis process.

Graphical abstract

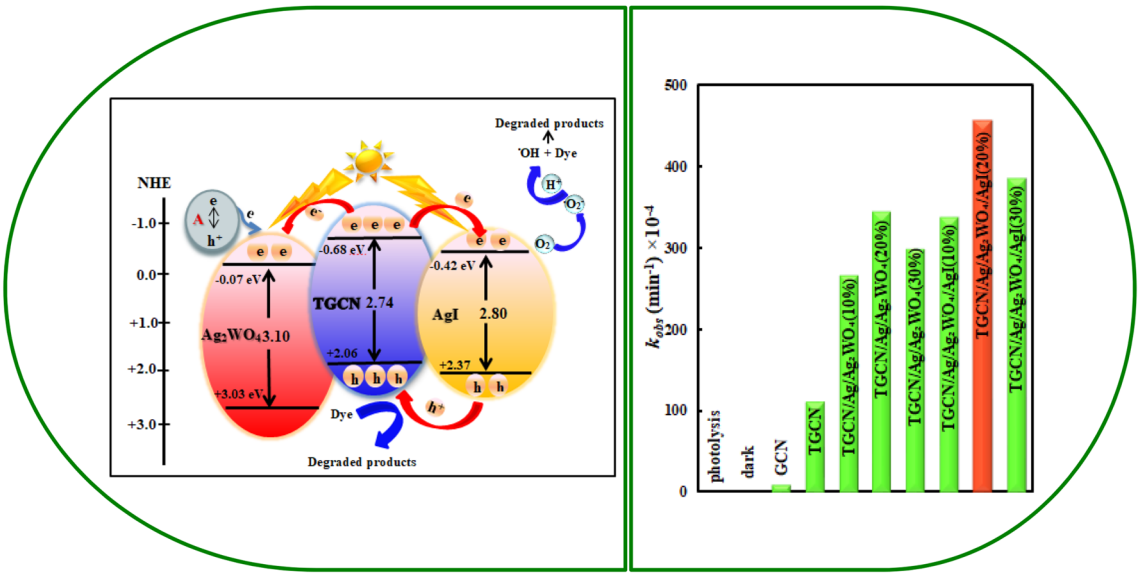

Keywords g-C_3N_4 tubular/Ag/Ag_2WO_4/AgI · Plasmonic photocayalyst · Tetracycline hydrochloride · Amoxicilline · Visible-light photocatalysis

Extended author information available on the last page of the article

1 Introduction

In recent years, environmental pollution has become one of the most important challenges of sustainable development. So far, various methods such as chemical, physical, and biological strategies have been used to eliminate pollutants. However, bottlenecks such as inefficient performance, high energy consumption, long processing time, and incomplete destruction exist in these processes, which hinder their widespread utilization [1, 2]. As a result, human societies have an immediate need for the development of an efficacious and economic technology to address the crises generated in the field of environment and energy. Degradation of various organic contaminants through advanced oxidation processes has been considered as a promising technology thanks to the advantages such as having simple processes, environmental friendliness, and working at ambient conditions [3, 4]. Among them, heterogeneous photocatalysts have attracted interest from worldwide research communities [5, 6]. The photocatalytic processes rely on extremely active species such as hydroxyl radicals ($^{\bullet}OH$), superoxide radicals ($^{\bullet}O_2^-$), and holes (h^+) produced after the absorption of light energy by the designed photocatalysts, which play a vital role in the degradation reactions.

Hitherto, very diverse semiconductors such as ZnO, TiO_2, SnO_2, CeO_2, Ag_2O, CuO, Cu_2O, BiOX (X is a halide), AgX, ZnS, CdS, SnS_2, Bi_2S_3, Ag_2S, Ag_3PO_4, and MFe_2O_4 (M = Ca, Mg, Zn, Co, Ni) have been utilized in the heterogeneous photocatalysis with the purpose of contaminant eliminations [7–10]. With the intention of extensive usage of solar energy in photocatalytic reactions, designing and manufacturing of efficacious photocatalysts activated under visible-light illumination are hot-spot research fields worldwide [11–14]. Recently, g-C_3N_4 (abbreviated as GCN) has received much attention for its excellent properties such as high photochemical stability, suitable bandgap, efficient visible-light response, and cheap price in the removal of wastewater contaminants [15, 16]. Because of some bottlenecks such as long electron transmission distance, limited surface area, and rapid combination of charge carriers, the photocatalytic performance of pristine GCN is poor [17, 18]. Thus, several methods have been suggested to tackle these drawbacks such as doping elements, production of GCN nanosheets, integration with other semiconductors, and combination with carbon-containing materials [19, 20]. The conversion of bulk GCN into tubular GCN (TGCN) is a promising method to improve the specific surface area and shorten the charge transfer path, which increases the active reaction sites and charge separation efficiency [21–23].

In this research paper, we designed plasmonic photocatalysts with high performance through adorning TGCN with Ag_2WO_4 and AgI nanoparticles with energy gaps of 3.10 and 2.60 eV, respectively. Decorations of these semiconductors were carried out using a facile ultrasonic-irradiation method. Interestingly, during the decoration of Ag_2WO_4 nanoparticles, some of the silver cations were reduced to metallic silver under ultrasonic irradiation. The reduction of silver cations takes place through reaction with hydrogen radicals, which are produced under ultrasonic irradiation [24]. Similar reductions reactions have been reported during the fabrication of various photocatalysts [25, 26]. Hence, plasmonic TGCN/Ag/Ag_2WO_4/AgI photocatalysts were fabricated and utilized for impressive photocatalyitc removal of tetracycline hydrochloride (TC), amoxicillin (AMX) (as usual antibiotics), methyl orange (MO) (as an anionic dye), methylene blue (MB), and fuchsine (as cationic dyes) under visible-light illumination.

2 Experimental section

2.1 Synthesis part

2.1.1 Synthesis of GCN and TGCN

The fabrication procedures of GCN and TGCN powders using melamine (Loba Chemise, 99.2%) were described in our previous work [27].

2.1.2 Synthesis of TGCN/Ag/Ag_2WO_4 (20%) nanocomposite

For the synthesis of TGCN/Ag/Ag_2WO_4 (20%) photocatalyst including 80 wt% TGCN and 20% Ag/Ag_2WO_4, 0.4 g of the TGCN was sonicated for 10 min into 150 mL water. Afterward, 0.073 g $AgNO_3$ was added in the suspension and stirred for 60 min. Then, sodium tungstate ($Na_2WO_4{\cdot}2H_2O$, 0.071 g in 20 mL water) was added drop by drop into the suspension and it was sonicated for 120 min. Ultimately, the centrifuged photocatalyst was dried after washing with water and ethanol.

2.1.3 Preparation of TGCN/Ag/Ag_2WO_4/AgI (20%) nanocomposite

For the synthesis of TGCN/Ag/Ag_2WO_4/AgI (20%) photocatalyst, in which 20% is wt% of AgI, 0.4 g of the TGCN/Ag/Ag_2WO_4 (20%) was dispersed in 150 mL water via sonication for 10 min followed by adding 0.072 g of $AgNO_3$ in the suspension. After stirring for 60 min, sodium iodide (0.063 g in 20 mL of water) was added drop by drop into the suspension and it was sonicated for 120 min. The prepared photocatalyst was washed and dried like in the previous section. The method utilized to fabricate the TGCN/Ag/Ag_2WO_4/AgI nanocomposites is illustrated in Scheme 1.

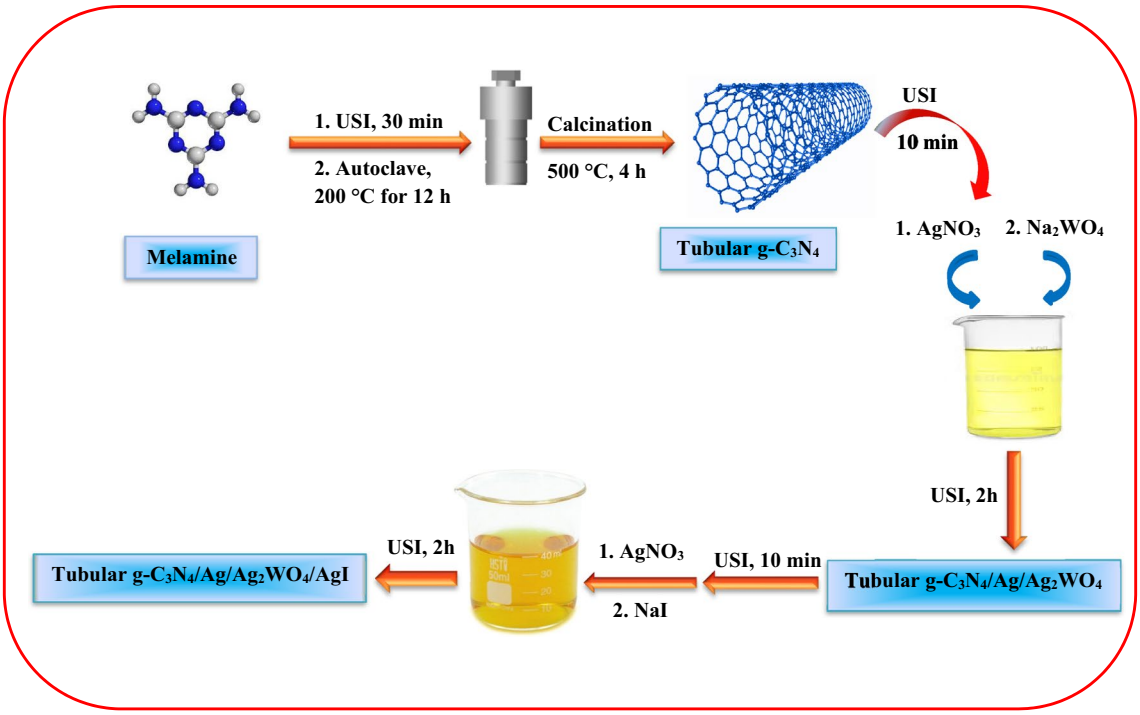

Scheme 1. Schematic presentation for the synthesis of g-C_3N_4 tubular/Ag/Ag_2WO_4/AgI systems

2.2 Characterization

The crystal planes of the materials were presented by X-ray (Philips Xpert) diffraction tests. The morphology and elemental composition were determined by an FESEM of model ZEISS G300. Ultraviolet–visible spectra of the materials were obtained using a Scinco 4100 spectrophotometer. The FT-IR spectroscopy was utilized to explore the functional groups by a Perkin Elmer Spectrum between 4000 and 400 cm^{-1}. The XPS of the optimum material was measured with an AXIS-Ultra X-ray photoelectron spectrometer (Kratos, DLD-600 W). The PL data were examined in a Perkin Elmer LS 55 spectrophotometer. The TGA was performed by Linseis STA PT 1000. The surface area of materials was obtained by BELSORP-mini II. The EIS and photocurrent measurements were performed with a three-electrode system using a mAutolabIII Potentiostat/Galvanostat by 0.5 M Na_2SO_4 as electrolyte, a saturated Ag/AgCl reference electrode and the desired photocatalyst as the working electrode. The working electrode was made of the photocatalyst using a fluorine-doped tin oxide conducting glass. In the photocurrent experiments, a 500 W Xe lamp by power density of 100 mW/cm^2 was utilized. Furthermore, in EIS experiments, the potential was 0.2 V.

2.3 Photoactivity analysis

The photoactivities were explored for TC (6.2×10^{-8} M), AMX (1×10^{-4} M), RhB, MB, MO (1×10^{-5} M), and fuchsine (8×10^{-6} M), through recording the absorption peaks at 357, 226, 553, 664, 477, and 540 nm, respectively, under LED lamp (50 W) supplying visible-light illumination. The detailed descriptions of photocatalysis experiments were reported elsewhere [27].

3 Results and discussion

The crystal phases of samples were collected by XRD and they are shown in Fig. 1. The XRD pattern of TGCN/Ag/Ag_2WO_4 (20%) nanocomposite shows the peaks of graphitic carbon nitride (JCPDS No. 871526), metallic silver (JCPDS No. 65-2871), and Ag_2WO_4 (JCPDS No. 33–1195) [28–30]. Also, about the TGCN/Ag/Ag_2WO_4/AgI (20%) nanocomposite, the peaks of cubic phase AgI are clearly visible (JCPDS No. 01-0503) [31]. Accordingly, the XRD analyses confirmed the production of TGCN/Ag/Ag_2WO_4/AgI (20%) nanocomposite without impurity peaks.

The elemental composition of the TGCN/Ag/Ag_2WO_4/AgI (20%) nanocomposite was analyzed by EDX spectrum,

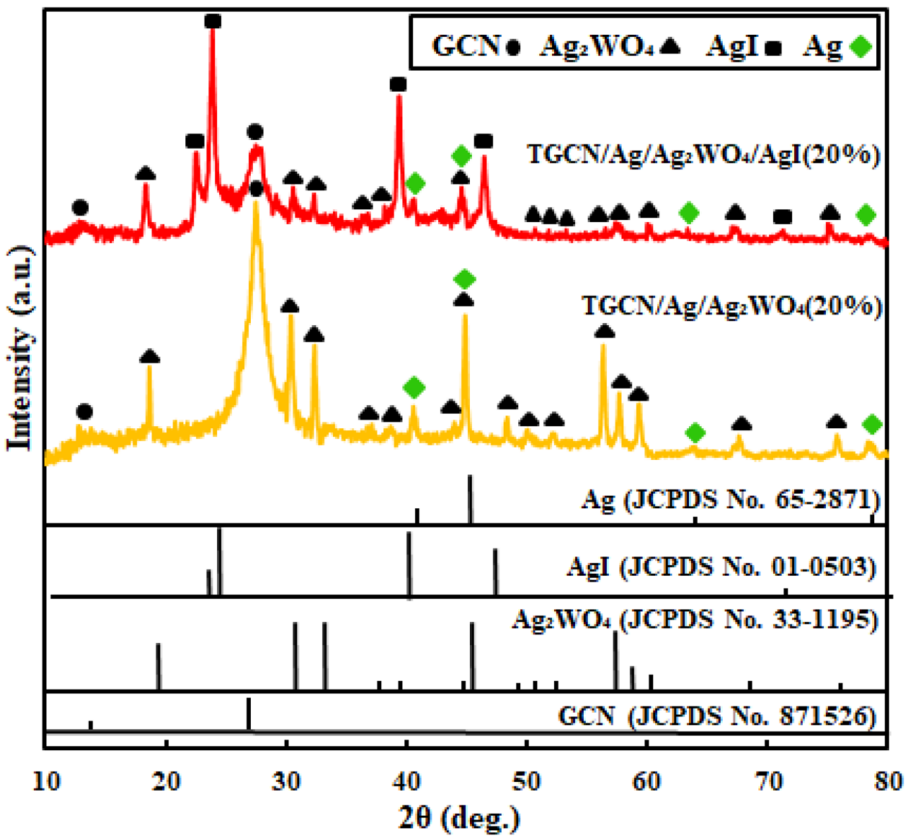

Fig. 1 XRD of as-designed photocatalysts

indicating C, N, O, Ag, W, and I elements (Fig. 2a). For perception the morphology, SEM image was provided. As seen in Fig. 2b, particles of Ag, Ag_2WO_4, and AgI anchored on the tubular graphitic carbon nitride, confirming integration of these components to collaborate in improving the photocatalytic activity.

To investigate the chemical status of the surface elements in the TGCN/Ag/Ag_2WO_4/AgI (20%) nanocomposite, XPS analyses were considered. As seen in Fig. 3a, the photocatalyst composed of C, N, O, Ag, W, and I elements, which are a match with the XRD and EDX tests. Figure 3b presents the spectrum for C1s with two distinct peaks at 288.1 and 284.6 eV ascribed to the sp^2–hybridized carbon bonded to the N of the trizine rings (N=C–N) and to the carbon atoms with C–C bond, respectively originated from TGCN [32]. In Fig. 3c, the peaks of 398.75 and 400.10 eV were observed, which were assigned to the N atoms presented in the C=N–C ring and sp^3 hybridized nitrogen N–$(C)_3$, respectively [33]. Furthermore, in Fig. 3d, the two peaks at 373.7 and 367.7 eV are typically relevant to Ag $3d_{3/2}$ and Ag $3d_{5/2}$ from Ag^+, and the peaks at 369.0 and 375.0 eV are assigned to Ag $3d_{5/2}$ and Ag $3d_{3/2}$ from metallic silver [34, 35]. The spectrum of W4f presents the peaks at 35.27 and 37.43 eV, matched to W $4f_{7/2}$ and W $4f_{5/2}$, respectively presented in WO_4^{2-} ions (Fig. 3e) [36]. In the case of iodide ions, two characteristic peaks at 619.78 and 631.28 eV were ascribed to I $3d_{5/2}$ and I $3d_{3/2}$, respectively (Fig. 3f) [37]. Finally, the XPS spectrum of O 1 s (Fig. 3g) shows that the peak at 530.50 eV is dependent on the lattice oxygen, while the peak at 532.50 eV derived from the oxygen of adsorbed water over the photocatalyst [38].

The FT-IR spectra are illustrated in Fig. 4a. As seen, the peak at 810 cm^{-1} is related to the vibration of the heptazine structure, which is assigned to the main unit of GCN [39]. In addition, many peaks appearing in the range of 1200–1650 cm^{-1} correspond to the C–N and C=N bonds in the GCN [40]. In these spectra, broad absorption bands positioned at 3000–3300 cm^{-1} are relevant to the N–H and O–H bonds [41, 42]. A new peak at 868 cm^{-1} is observed for the TGCN/Ag/Ag_2WO_4 (20%) and TGCN/Ag/Ag_2WO_4/AgI (20%) nanocomposites, which is assigned to the asymmetric tensile vibration of the O–W–O group [43]. Thus, the characteristic peaks of GCN and Ag_2WO_4 semiconductors are visible in the spectra. Finally, similar to AgI-based photocatalysts, the vibration peak for AgI was not detected [44]. The optical characteristics of materials were investigated by UV–vis DRS measurements. Compared to the GCN, TGCN shows a blue-shifted absorption, which is related to the confinement effect [27, 45]. As observed, the TGCN/Ag/Ag_2WO_4 nanocomposites show much higher absorption in the visible region because of the presence of metallic silver [46]. Most importantly, in the TGCN/Ag/Ag_2WO_4/AI

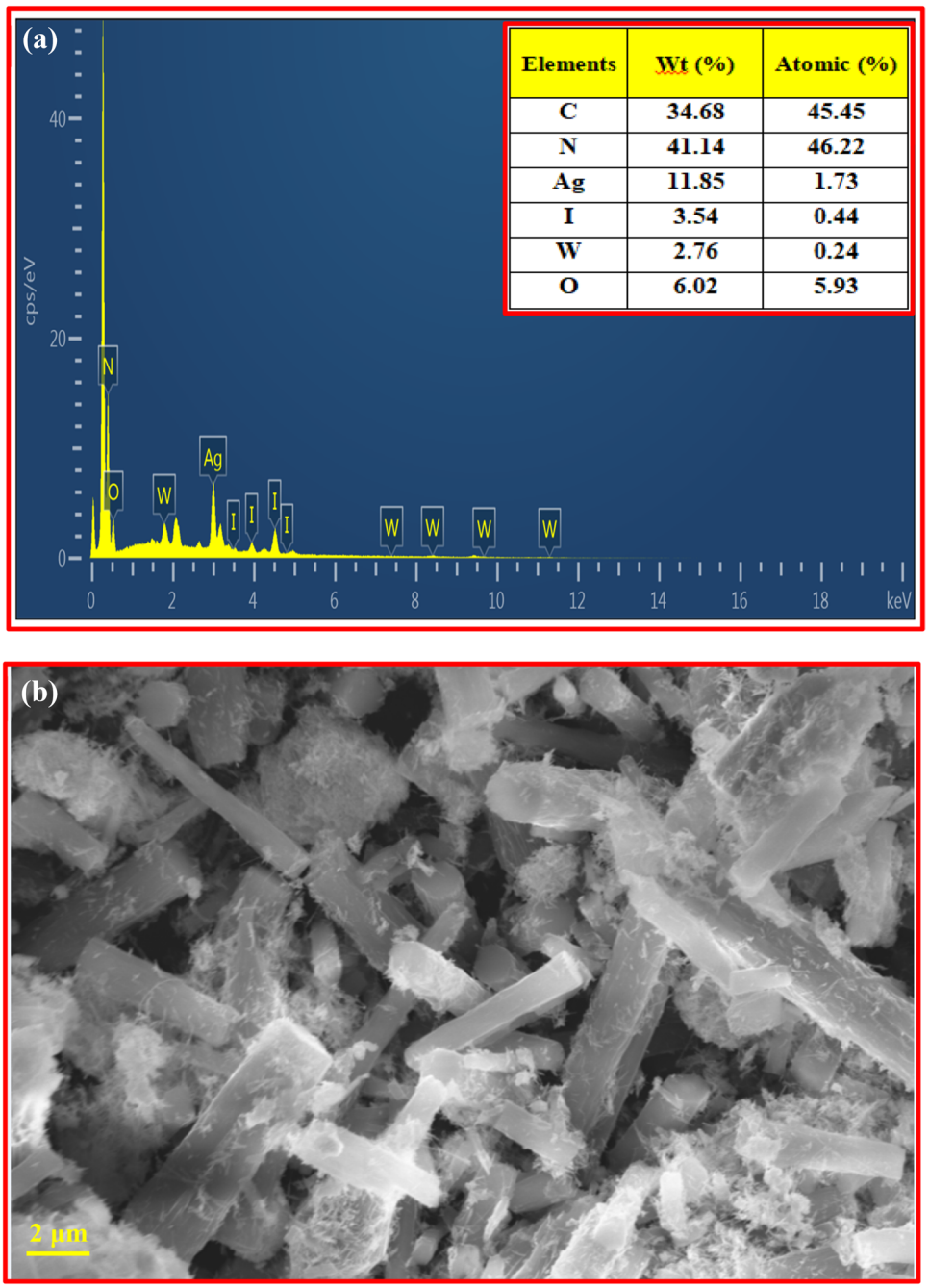

Fig. 2 **a** EDX and **b** SEM of TGCN/Ag/Ag_2WO_4/AgI (20%) nanocomposite

nanocomposites, the absorption intensity was stronger in the visible region than the other materials thanks to the presence of small bandgap AgI and plasmonic characteristics of Ag, indicating the production of more charge carriers in the visible area.

As known, TGA is a thermal analysis method utilized for the evaluation of the thermal stability of materials. As seen in Fig. 5a, significant weight loss in the materials started from almost 500 °C. It is evident that by converting GCN to TGCN and decorating Ag_2WO_4 and AgI, the thermal stability of the materials decreased [47]. Using the remained weights after heating the TGCN/Ag/Ag_2WO_4 (20%) and TGCN/Ag/Ag_2WO_4/AgI (20%) nanocomposites up to 700 °C, the contents of TGCN in these photocatalysts were obtained as 80.4 and 58.8%, respectively. The BET-specific areas of the materials were measured by N_2 sorption curves, as shown in Fig. 5b. Based on the IUPAC classification, the isotherms are type II with H3 hysteresis hoops. The surface areas of GCN, TGCN, TGCN/Ag/Ag_2WO_4 (20%), and TGCN/Ag/Ag_2WO_4/AgI (20%) materials were reported as 12.4, 53.2, 6.98, and 9.69 m^2/g, respectively. Therefore, the specific surface area of the nanocomposites decreased by

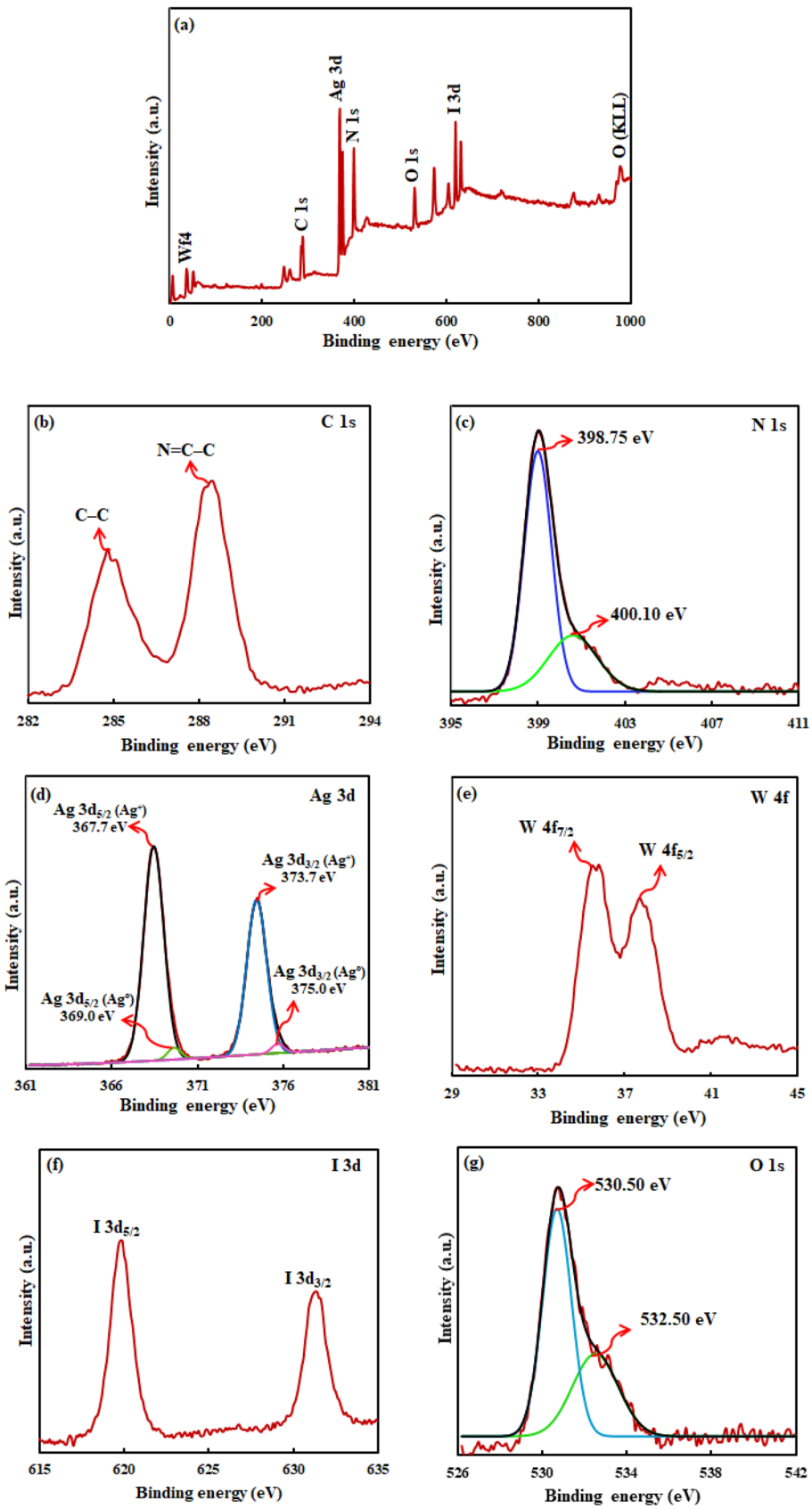

Fig. 3 The XPS spectra of TGCN/Ag/Ag_2WO_4/AgI (20%): **a** Survey scan, **b**–**g** C 1 s, N 1 s, Ag 3d, W 4f, I 3d, and O 1 s

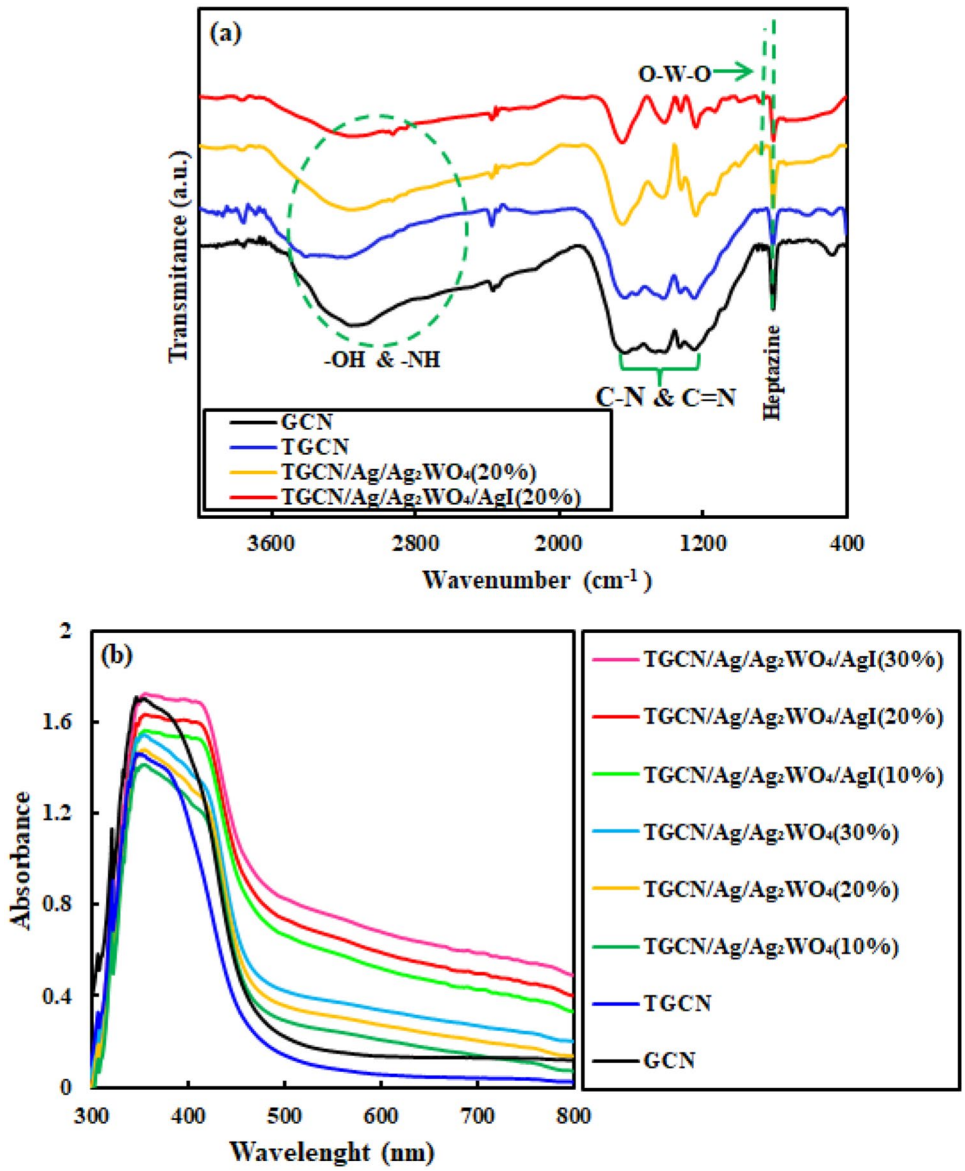

Fig. 4 **a** FT-IR and **b** UV–vis DR spectra of the photocatalysts

anchoring Ag_2WO_4, Ag, and AgI particles over the TGCN, because of occupying some active points by deposited materials. Consequently, the surface area of the nanocomposites could not have a role in the acceleration of the degradation reaction relative to the GCN and TGCN photocatalysts.

Tetracycline hydrochloride is one of the widely used antibiotics, which contaminante our environment. As shown in Fig. 6a, destruction of this antibiotic is very difficult without using any photocatalyst under visible-light illumination, because of its high chemical stability. But, over the GCN, almost 24% of TC was degraded after the light irradiation for 90 min. After converting GCN to TGCN, the photocatalytic performance improved significantly by degrading about 55% of the antibiotic at the same time. It is noteworthy that when TGCN was adorned by Ag_2WO_4, Ag, and AgI, the photocatalytic activity was impressively promoted and about 87.4% and 99% of TC were degraded over the TGCN/Ag/Ag_2WO_4 (20%) and TGCN/Ag/Ag_2WO_4/AgI (20%) nanocomposites, respectively. The kinetic constants for the photocatalytic removal of TC were estimated by pseudo-first-order kinetic equation. As illustrated in Fig. 6b, the TGCN/Ag/Ag_2WO_4/AgI (20%) photocatalyst has the highest kinetic constant of 457×10^{-4} min^{-1}, which is 45.6, 4.03, and 1.32-folds higher than the GCN, TGCN, and TGCN/Ag/Ag_2WO_4 (20%) photocatalysts, respectively. As seen, the TGCN/Ag/Ag_2WO_4/AgI (30%) photocatalyst showed poor activity than the TGCN/Ag/Ag_2WO_4/AgI (20%) nanocomposite, because excessive addition of AgI nanoparticles could destruct the heterojunctions among the components through accumulation and poor dispersion of the nanoparticles over the TGCN, resulting in decreased activity.

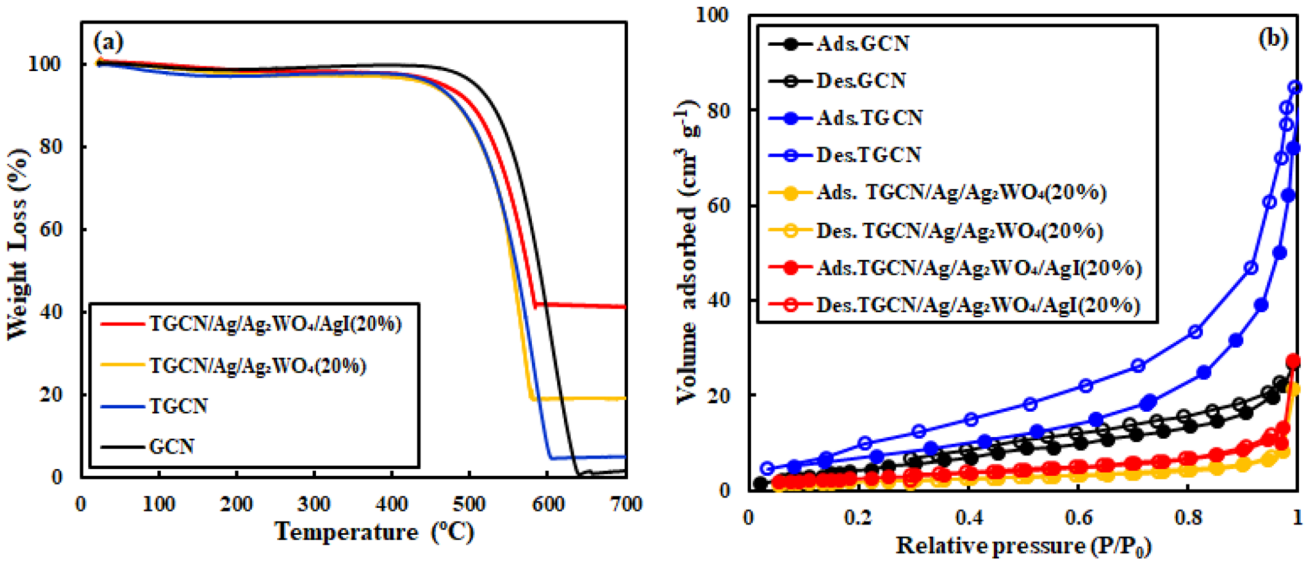

Fig. 5 **a** TGA and **b** BET analyses for the prepared materials

To study the mechanism insight the highly promoted photocatalytic activity, PL, EIS, and photocurrent analyses were provided, as seen in Fig. 7a. The order of PL intensities is as GCN > TGCN > TGCN/Ag/Ag_2WO_4 (20%) > TGCN/Ag/Ag_2WO_4/AgI (20%). Due to the much pronounced diminish of the PL intensity, it was concluded that the segregation of electron/hole pairs in the TGCN/Ag/Ag_2WO_4/AgI (20%) nanocomposite is much higher than the specified materials. In addition to the charges production, their migration and transfer to the catalyst surface for participation in the redox reactions play a vital role in the improvement of the activity [48, 49]. As seen in the EIS of the GCN, TGCN, TGCN/Ag/Ag_2WO_4 (20%), and TGCN/Ag/Ag_2WO_4/AgI (20%) materials, the TGCN/Ag/Ag_2WO_4/AgI (20%) nanocomposite has the smallest arc radius among the photocatalysts, implying that the generated charges could easily reach to the catalyst surface thanks to its low resistance for migration of charges (Fig. 7b). To further confirm the above results, the transient photocurrent responses were evidenced for several on–off cycles under visible light (Fig. 7c). As expected, the TGCN/Ag/Ag_2WO_4/AgI (20%) nanocomposite exhibited an extremely high photocurrent response than other materials. Therefore, it was clearly confirmed that a lot of charge carriers in the TGCN/Ag/Ag_2WO_4/AgI (20%) nanocomposite are produced, and they migrated rapidly to the catalyst surface to participate in the photocatalytic degradation of the specified antibiotic, as observed by greatly improved photocatalytic performance.

Inhibition experiments were performed to identify different types of species in TC degradation. Hence, ammonium oxalate (AO), benzoquinone (BQ), and 2-PrOH were selected as the scavengers of h^+, $^{\bullet}O_2^-$, and $^{\bullet}OH$, respectively. As seen in Fig. 8a, in the presence of AO, BQ, and 2-PrOH, the degradation constant were reduced to 29.8×10^{-4}, 25.2×10^{-4}, and 300×10^{-4}, respectively. Therefore, $^{\bullet}O_2^-$ and h^+ play a chief role in the degradation process under visible light.

The flat-band potential (E_{fb}) of a semiconductor can be appraised by Mott-Schottky plot. Figure 8b shows the plots for TGCN, Ag_2WO_4 and AgI semiconductors. As presented, these semiconductors show a positive slope, which confirm that these materials have n-type semiconducting characteristics. Based on these plots, E_{fb} for TGCN (–0.78 V vs. Ag/AgCl; -0.58 V vs. NHE), Ag_2WO_4 (– 0.17 V vs. Ag/AgCl) and AgI (– 0.52 V vs. Ag/AgCl) were obtained. As known, for n-type semiconductors, E_{fb} is about 0.1 V lowers than the conduction band potentials (E_{CB}) [50]. Therefore, the E_{CB} of TGCN, Ag_2WO_4, and AgI were computed to be – 0.88, – 0.27 and – 0.62 V (vs. Ag/AgCl). After converting the potentials to the NHE scale using $E_{NHE} = E_{Ag/AgCl} + 0.2$ [51], the E_{CB} of TGCN, Ag_2WO_4, and AgI can be estimated to – 0.68, – 0.07 and – 0.42 eV and the E_{VB} of them were obtained to be 2.06, 3.03, and 2.37 eV, respectively using the equation $E_{VB} = E_{CB} + E_g$.

As shown in Fig. 9, a possible mechanism for impressive improvement of the photocatalytic capability of TGCN/Ag/Ag_2WO_4/AgI nanocomposites was proposed. As medium band-gap materials, electron/hole pairs are produced over TGCN and AgI under visible light. The CB potential of TGCN is more negative than Ag_2WO_4 and

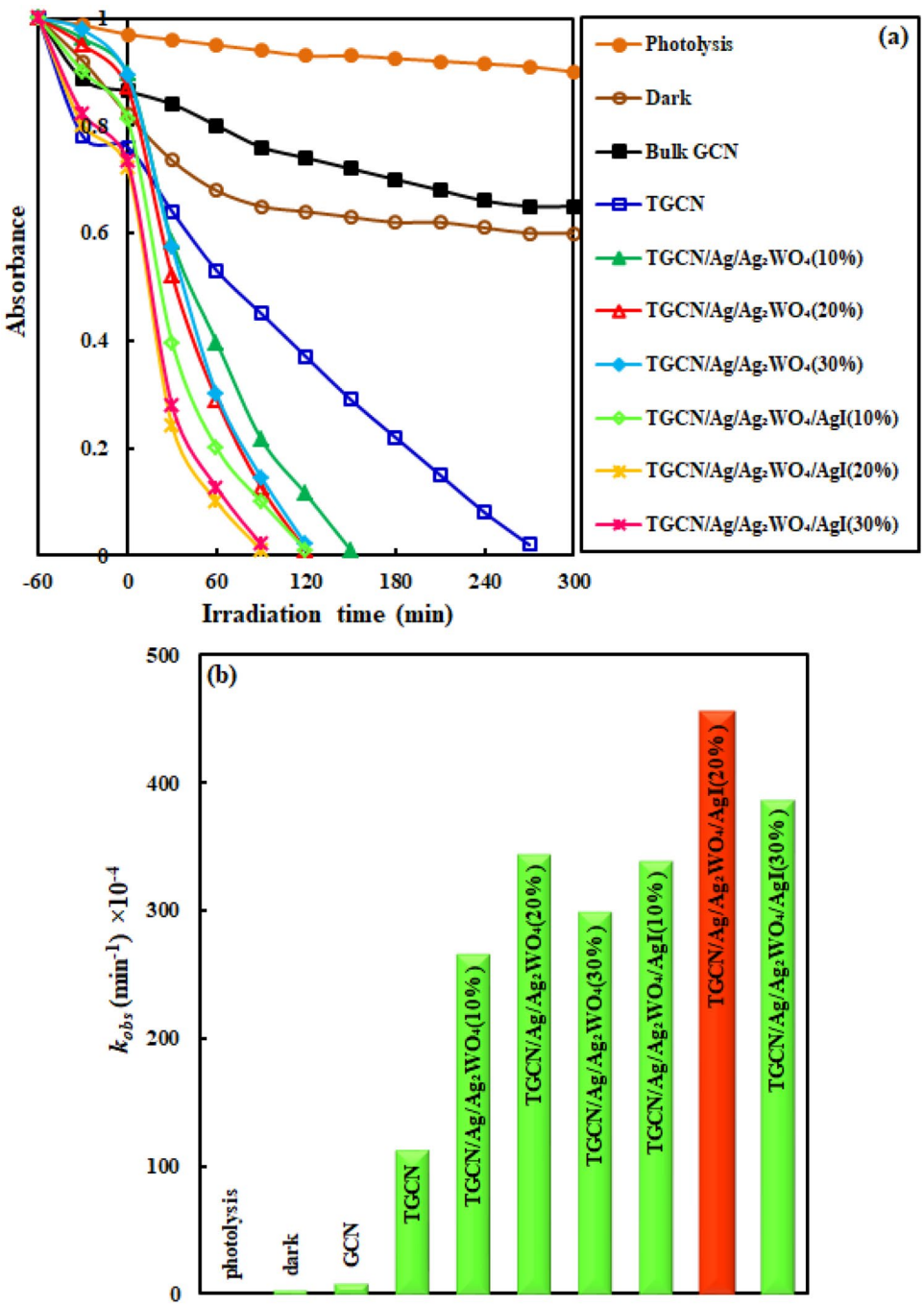

Fig. 6 **a** Photodegradation and **b** kinetic rate constants for tetracycline over the prepared materials

AgI semiconductors. Accordingly, the created electrons on TGCN easily migrate to the CB of Ag_2WO_4 and AgI. Inversely, the generated holes over the VB of AgI transmit unto the VB of TGCN, thanks to the more positive potential of the holes in AgI. The electrons accumulated in the CB of TGCN and AgI were attracted with oxygen to form $^{\bullet}O_2^-$, since the standard potential of $O_2/^{\bullet}O_2^-$ (−0.33 eV) is more positive than the CB potentials of the mentioned materials [52]. Additionally, the electrons on the CB of Ag_2WO_4 could be gained by oxygen to generate $^{\bullet}OH$ ($E°(O_2/H_2O_2) = +0.682$ eV vs. NHE). Subsequently, the generated H_2O_2 and $^{\bullet}O_2^-$ species react with pollutant species to degrade them. Moreover, the holes in VB of TGCN are not positive sufficient to oxidize $H_2O/^-OH$ to generate $^{\bullet}OH$ radicals ($E°_{H2O/OH°} = +2.72$ eV, $E°_{-OH/OH°} = +2.38$ eV) [53]. Then, the produced holes at the VB of TGCN react

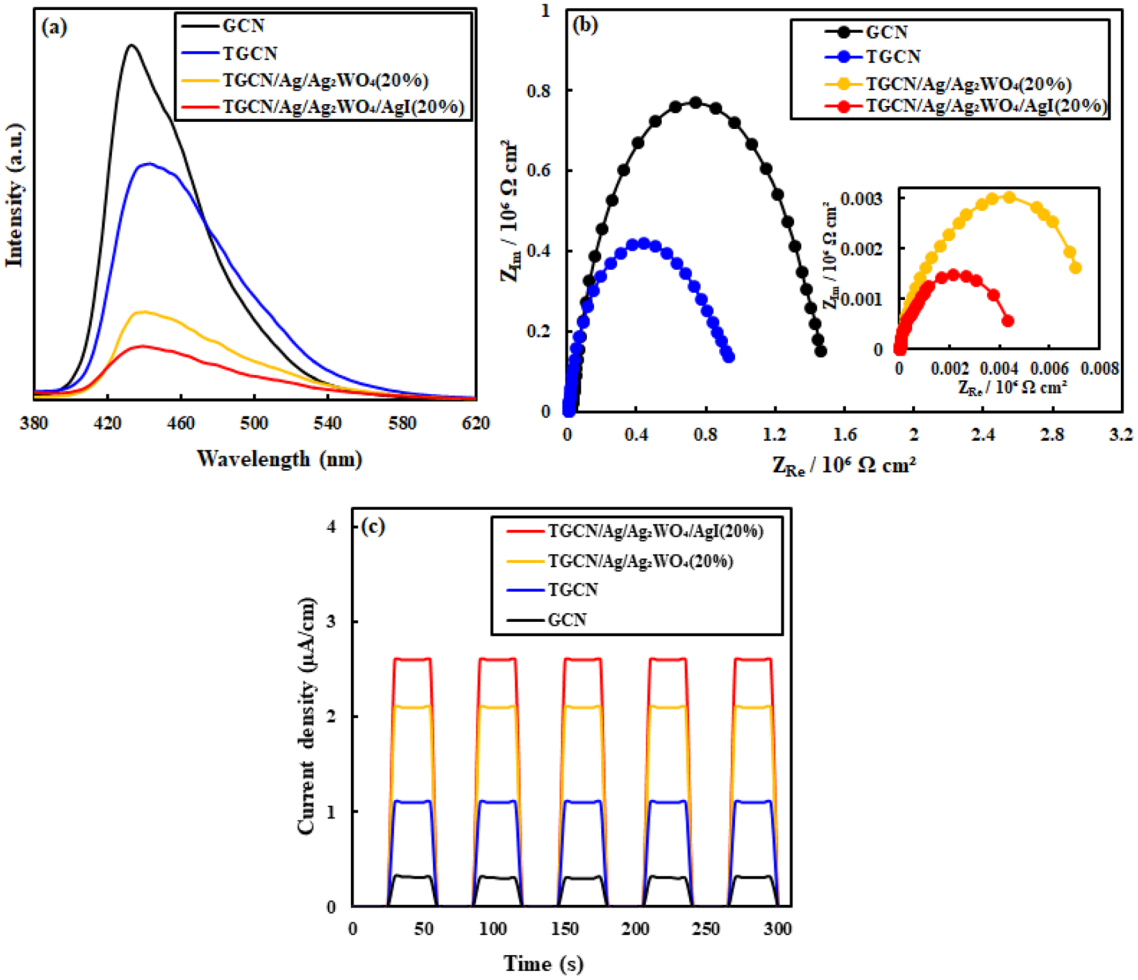

Fig. 7 **a** PL, **b** EIS, and **c** transient photocurrents for the materials

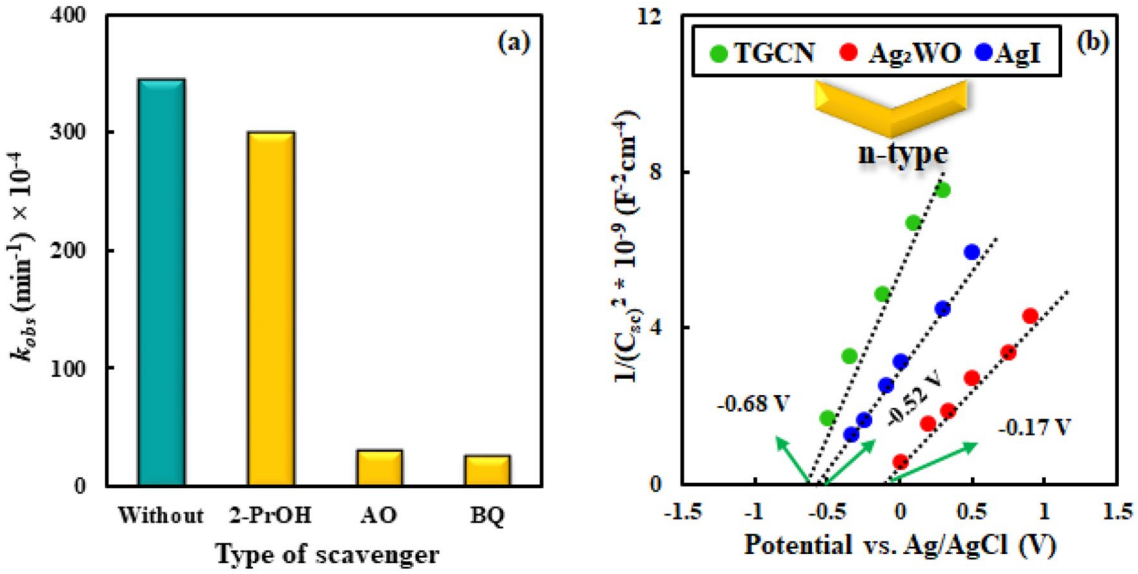

Fig. 8 **a** Effect of scavengers on the photocatalytic ability of TGCN/Ag/Ag_2WO_4/AgI (20%) in TC degradation and **b** Mott-Schottky plots for TGCN, Ag_2WO_4 and AgI

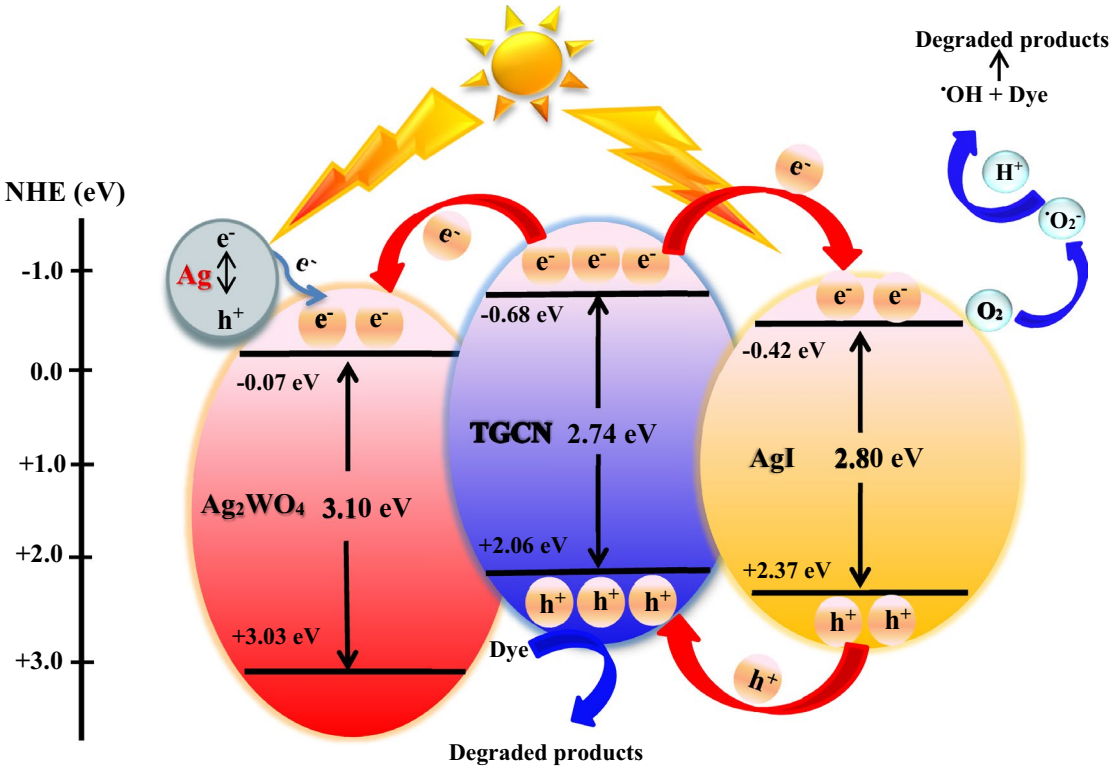

Fig. 9 The segregation mechanism of charge carriers in the TGCN/Ag/Ag_2WO_4/AgI photocatalysts

with pollutants and oxidize them to different products. In summary, appropriate band energies of TGCN, Ag_2WO_4, and AgI components and the presence of metallic silver facilitate segregation of the generated charges, resulting in impressive photocatalytic activity. In addition, the presence of metallic silver and medium band gap semiconductors (TGCN and AgI) in the structure of the photocatalyst help to generate a large number of charges under visible light to participate in the degradation reactions [53].

The stability and recyclability of a photocatalyst have a great role in its widespread usage. Figure 10a shows the repeated application of the TGCN/Ag/Ag_2WO_4/AgI (20%) nanocomposite for the elimination of TC under visible light. As illustrated, the photocatalyst has enough stability for four photocatalytic runs with a small decrease in the activity. Therefore, the nanocomposite is considered as a stable photocatalyst for environmental applications. Furthermore, as seen in Fig. 10b, the XRD pattern of the photocatalyst does not show any change in the phase and structure after the repeated degradation reaction. These results disclose that the TGCN/Ag/Ag_2WO_4 (20%) nanocomposite is stable and it has high durability during photocatalytic reactions. In addition, in Fig. 10c, the SEM image of the nanocomposite after the photocatalytic reaction is shown. By comparison between Fig. 2b and this figure, it is inferred that the nanocomposite retained its morphology during the degradation reaction.

For representing the ability of TGCN/Ag/Ag_2WO_4/AgI (20%) nanocomposite for photocatalytic removal of different pollutants, the degradation of AMX, RhB, MB, MO, and fuchsine were conducted and the results are displayed in Fig. 11. Among these contaminants, RhB, MB, and Fuchsine have cationic and MO has anionic characteristics and amoxicillin (AMX) is an antibiotics. As detected, the activity of TGCN/Ag/Ag_2WO_4/AgI (20%) nanocomposite for the elimination of AMX, RhB, MB, MO, and fuchsine are 9.78, 4.21, 3.25, 4.97, and 5.18-folds higher than the TGCN and 14.7, 52.2, 7.46, 9.79, and 13.2-folds as much as GCN, respectively. Hence, the TGCN/Ag/Ag_2WO_4/AgI (20%) nanocomposite shows significant photocatalytic activity in degradation of different water pollutants.

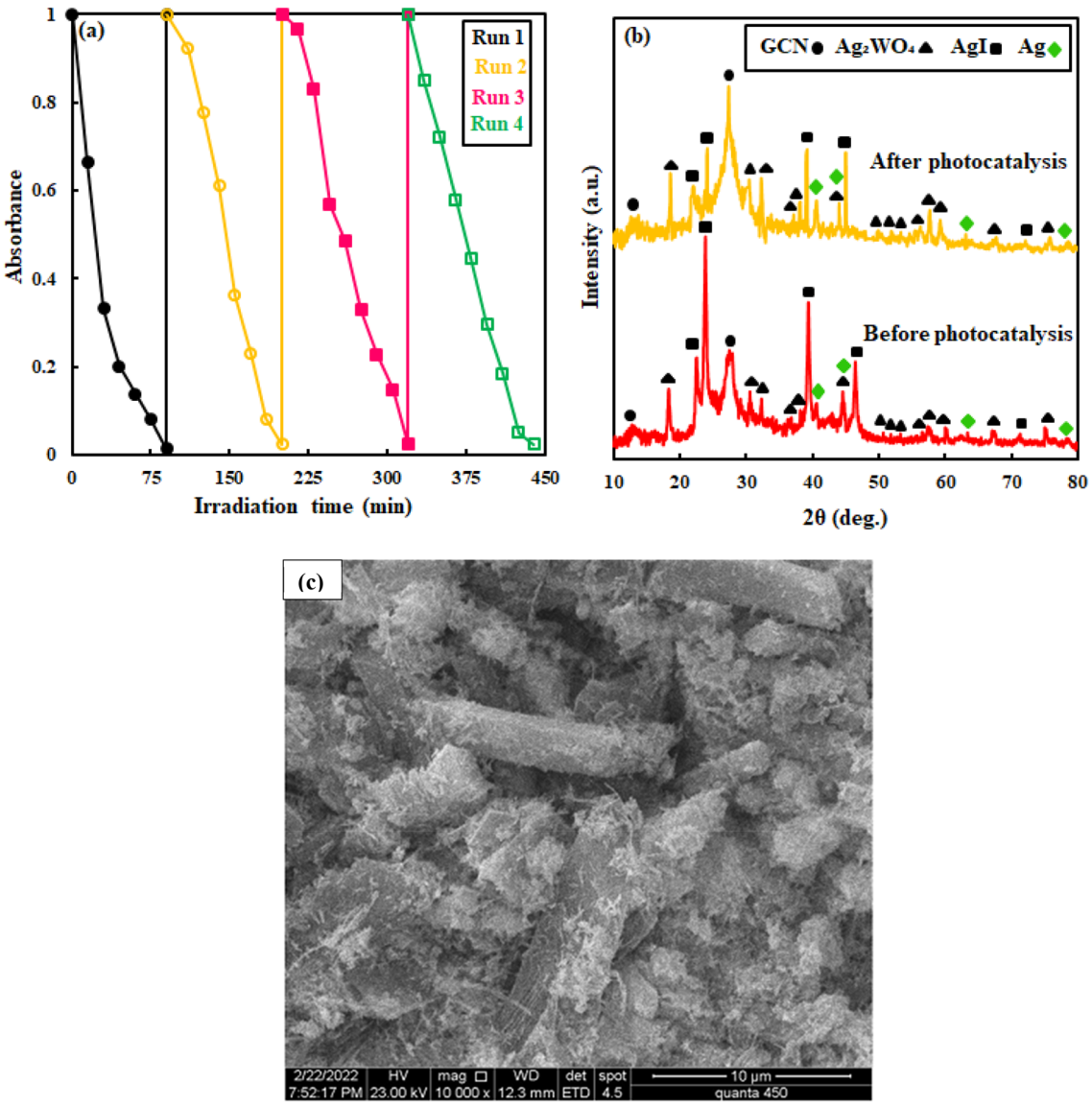

Fig. 10 **a** Reusability of the TGCN/Ag/Ag_2WO_4/AgI (20%) system, **b** XRD patterns of the TGCN/Ag/Ag_2WO_4/AgI (20%) nanocomposite before and after photocatalysis and **c** SEM image of the nanocomposite after photocatalytic reaction

4 Conclusion

In summary, novel plasmonic TGCN/Ag/Ag_2WO_4/AgI photocatalysts were synthesized by an ultrasonic-assisted procedure. The fabricated plasmonic photocatalyst illustrated remarkable performance in the degradation of different pollutants including two antibiotics and four dye pollutants. The incremented activity of TGCN/Ag/Ag_2WO_4/AgI (20%) nanocomposite in the removal of TC was about 1.32, 4.03, and 45.6-folds as high as the TGCN/Ag/Ag_2WO_4 (20%), TGCN, and GCN photocatalysts, respectively. Moreover, the photoactivity of TGCN/Ag/Ag_2WO_4/AgI (20%) nanocomposite in the removal of AMX, RhB, MB, MO, and fuchsine was 9.78, 4.21, 3.25, 4.97, and 5.18-folds premier than TGCN, and 14.7, 52.2, 7.46, 9.79, and 13.2-folds as high as GCN, respectively. According to the reactive-species-trapping tests, it was displayed that $^{\bullet}O_2^-$ and h^+ were generated and had a vital role in photocatalytic performance. The enhanced activity of the rational designed plasmonic photocatalyst was attributed to more production and promoted segregation of charges, thanks to the presence of metallic silver, two medium band-gap energy components, and appropriate band-energy alignment in the nanocomposite.

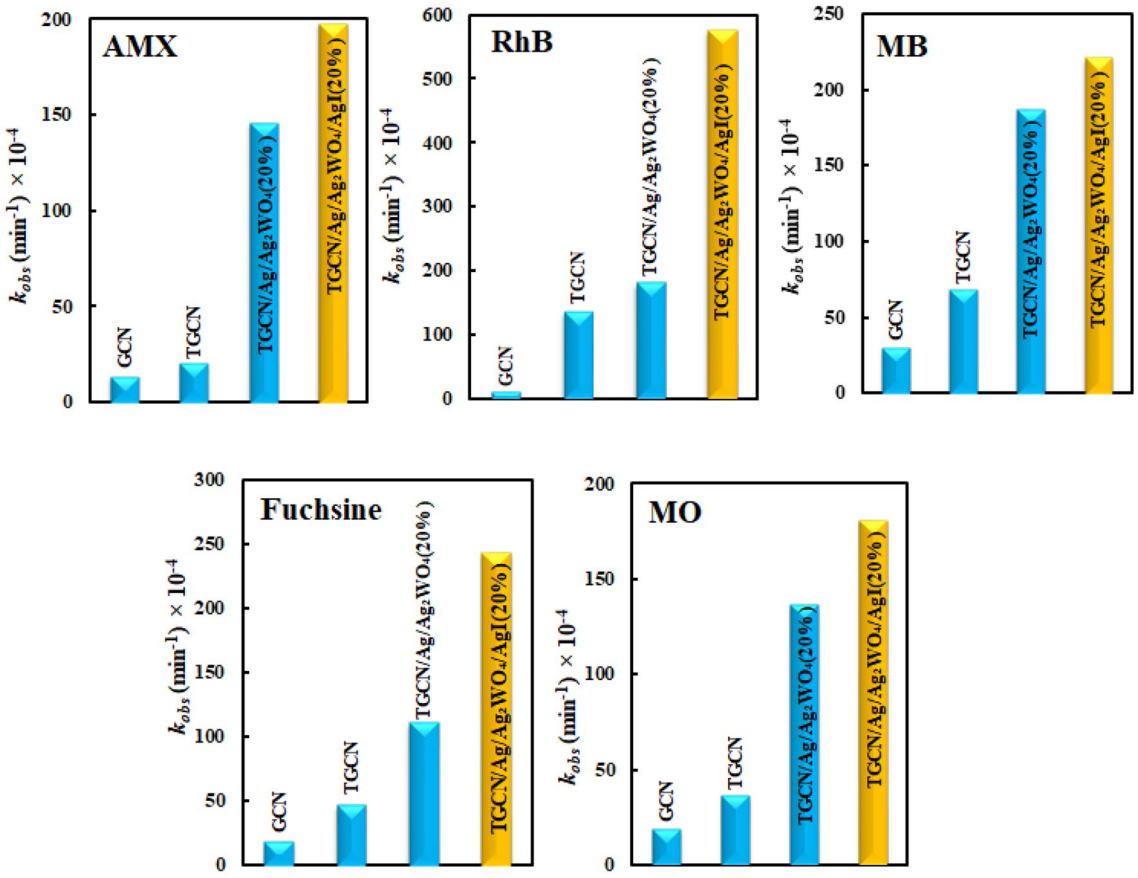

Fig. 11 The degradation rate constants of AMX, RhB, MB, fuchsine, and MO over the specified materials

Acknowledgements The authors acknowledge the University of Mohaghegh Ardabili, for any provided support.

Author contributions PH-E: Validation; formal analysis; investigation; resources; writing-original draft. AH-Y: conceptualization; methodology; writing—review and editing; supervision; project administration. XX: formal analysis; writing-review and editing. CW: formal analysis; writing—review and editing. AK: formal analysis; review and editing.

Declarations

Conflict of interest The authors declare that they have no known competing financial interests or personal relationships that could have appeared to influence the work reported in this paper.

References

1. Singh, P., Shandilya, P., Raizada, P., Sudhaik, A., Rahmani-Sani, A., & Hosseini-Bandegharaei, A. (2020). Review on various strategies for enhancing photocatalytic activity of graphene based nanocomposites for water purification. *Arabian Journal of Chemistry, 13*, 3498–3520.
2. Long, C., Jiang, Z., Shangguan, J., Qing, T., Zhang, P., & Feng, B. (2021). Applications of carbon dots in environmental pollution control: A review. *Chemical Engineering Journal, 406*, 126848.
3. Miklos, D. B., Remy, C., Jekel, M., Linden, K. G., Drewes, J. E., & Hübner, U. (2018). Evaluation of advanced oxidation processes for water and wastewater treatment—A critical review. *Water Research, 139*, 118–131.
4. Liu, H., Wang, C., & Wang, G. (2020). Photocatalytic advanced oxidation processes for water treatment: Recent advances and perspective. *Chemistry–An Asian Journal, 15*, 3239–3253.
5. Matafonova, G., & Batoev, V. (2018). Recent advances in application of UV light-emitting diodes for degrading organic pollutants in water through advanced oxidation processes: A review. *Water Research, 132*, 177–189.
6. Anandan, S., Ponnusamy, V. K., & Ashokkumar, M. (2020). A review on hybrid techniques for the degradation of organic pollutants in aqueous environment. *Ultrasonics Sonochemistry, 67*, 105130.
7. Raizada, P., Sudhaik, A., & Singh, P. (2019). Photocatalytic water decontamination using graphene and ZnO coupled photocatalysts: A review. *Materials Science for Energy Technologies, 2*, 509–525.
8. Chaibakhsh, N., & Moradi-Shoeili, Z. (2019). Enzyme mimetic activities of spinel substituted nanoferrites (MFe_2O_4), a review of synthesis, mechanism and potential applications. *Materials Science and Engineering: C, 99*, 1424–1447.
9. Chen, D., Cheng, Y., Zhou, N., Chen, P., Wang, Y., Li, K., & Huo, S. (2020). Photocatalytic degradation of organic pollutants using TiO_2-based photocatalyst: A review. *Journal of Cleaner Production, 268*, 121725.
10. Sun, C., Yang, J., Xu, M., Cui, Y., Ren, W., Zhang, J., Zhao, H., & Liang, B. (2021). Recent intensification strategies of SnO_2-based

photocatalysts: A review. *Chemical Engineering Journal, 427*, 131564.
11. Madi, M., Tahir, M., & Tasleem, S. (2021). Advances in structural modification of perovskite semiconductors for visible-light assisted photocatalytic CO_2 reduction to renewable solar fuels: A review. *Journal of Environmental Chemical Engineering, 9*, 106264.
12. Arunachalam, P., Nagai, K., Amer, M. S., Ghanem, M. A., Ramalingam, R. J., & Al-Mayouf, A. M. (2021). Recent developments in the use of heterogeneous semiconductor photocatalyst based materials for a visible-light-induced water-splitting system—A brief review. *Catalysts, 11*, 160.
13. Ekande, O. S., & Kumar, M. (2021). Review on polyaniline as reductive photocatalyst for the construction of the visible light active heterojunction for the generation of reactive oxygen species. *Journal of Environmental Chemical Engineering, 9*, 105725.
14. Tian, D., Zhou, H., Zhang, H., Zhou, P., You, J., Gang, Y., Pan, Z., Liu, Y., & Lai, B. (2021). Heterogeneous photocatalyst-driven persulfate activation process under visible light irradiation: From basic catalyst design principles to novel enhancement strategies. *Chemical Engineering Journal, 428*, 131166.
15. Song, B., Zeng, Z., Zeng, G., Gong, J., Xiao, R., Ye, S., Chen, M., Lai, C., Xu, P., & Tang, X. (2019). Powerful combination of g-C_3N_4 and LDHs for enhanced photocatalytic performance: A review of strategy, synthesis, and applications. *Advances in Colloid and Interface Science, 272*, 101999.
16. Patnaik, S., Sahoo, D. P., & Parida, K. (2020). Recent advances in anion doped g-C_3N_4 photocatalysts: A review. *Carbon, 172*, 682–711.
17. Zhang, S., Gu, P., Ma, R., Luo, C., Wen, T., Zhao, G., Cheng, W., & Wang, X. (2019). Recent developments in fabrication and structure regulation of visible-light-driven g-C_3N_4-based photocatalysts towards water purification: A critical review. *Catalysis Today, 335*, 65–77.
18. Mishra, A., Mehta, A., Basu, S., Shetti, N. P., Reddy, K. R., & Aminabhavi, T. M. (2019). Graphitic carbon nitride (g–C_3N_4)–based metal-free photocatalysts for water splitting: A review. *Carbon, 149*, 693–721.
19. Zhang, C., Li, Y., Shuai, D., Shen, Y., Xiong, W., & Wang, L. (2019). Graphitic carbon nitride (g-C_3N_4)-based photocatalysts for water disinfection and microbial control: A review. *Chemosphere, 214*, 462–479.
20. Zhang, M., Yang, Y., An, X., & Hou, L.-A. (2021). A critical review of g-C_3N_4-based photocatalytic membrane for water purification. *Chemical Engineering Journal, 412*, 128663.
21. Wang, W., Zeng, Z., Zeng, G., Zhang, C., Xiao, R., Zhou, C., Xiong, W., Yang, Y., Lei, L., Liu, Y., Huang, D., Cheng, M., Yang, Y., Fu, Y., Luo, H., & Zhou, Y. (2019). Sulfur doped carbon quantum dots loaded hollow tubular g-C_3N_4 as novel photocatalyst for destruction of *Escherichia coli* and tetracycline degradation under visible light. *Chemical Engineering Journal, 378*, 122132.
22. Liang, Q., Liu, X., Wang, J., Liu, Y., Liu, Z., Tang, L., Shao, B., Zhang, W., Gong, S., Cheng, M., He, Q., & Feng, C. (2021). In-situ self-assembly construction of hollow tubular g-C_3N_4 isotype heterojunction for enhanced visible-light photocatalysis: Experiments and theories. *Journal of Hazardous Materials, 401*, 123355.
23. Wang, S., Zhang, J., Li, B., Sun, H., & Wang, S. (2021). Engineered graphitic carbon nitride-based photocatalysts for visible-light-driven water splitting: A Review. *Energy & Fuels, 35*, 6504–6526.
24. Restrepo, C. V., & Villa, C. C. (2021). Synthesis of silver nanoparticles, influence of capping agents, and dependence on size and shape A review. *Environmental Nanotechnology, Monitoring & Management, 15*, 100428.
25. Naghizadeh-Alamdari, S., Habibi-Yangjeh, A., & Pirhashemi, M. (2015). One-pot ultrasonic-assisted method for preparation of Ag/AgCl sensitized ZnO nanostructures as visible-light-driven photocatalysts. *Solid State Sciences, 40*, 111–120.
26. Pirhashemi, M., & Habibi-Yangjeh, A. (2017). Ultrasonic-assisted preparation of plasmonic ZnO/Ag/Ag2WO4 nanocomposites with high visible-light photocatalytic performance for degradation of organic pollutants. *Journal of Colloid and Interface Science, 491*, 216–229.
27. Hemmati-Eslamlu, P., Habibi-Yangjeh, A., Asadzadeh-Khaneghah, S., Chand, H., & Krishnan, V. (2021). Integration g-C_3N_4 nanotubes and Sb_2MoO_6 nanoparticles, Impressive photoactivity for tetracycline degradation, Cr (VI) reduction, and organic dyes removals under visible light. *Advanced Powder Technology, 32*, 2322–2335.
28. Mei, F., Zhang, J., Liang, C. H., & Dai, K. (2021). Fabrication of novel CoO/porous graphitic carbon nitride S-scheme heterojunction for efficient CO_2 photoreduction. *Materials Letters, 282*, 128722.
29. Kalaivani, R., Maruthupandy, M., Muneeswaran, T., Hameedha Beevi, A., Anand, M., Ramakritinan, C. M., & Kumaraguru, A. K. (2018). Synthesis of chitosan mediated silver nanoparticles (Ag NPs) for potential antimicrobial applications. *Frontiers in Laboratory Medicine, 2*, 30–35.
30. Zhou, L., Li, Y., Yang, S., Zhang, M., Wu, Z., Jin, R., & Xing, Y. (2021). Preparation of novel 0D/2D Ag_2WO_4/WO_3 Step-scheme heterojunction with effective interfacial charges transfer for photocatalytic contaminants degradation and mechanism insight. *Chemical Engineering Journal, 420*, 130361.
31. Ghanbari, M., Soofivand, F., & Salavati-Niasari, M. (2016). Simple synthesis and characterization of Ag_2CdI_4/AgI nanocomposite as an effective photocatalyst by co-precipitation method. *Journal of Molecular Liquids, 223*, 21–28.
32. Chen, Z., Guo, F., Sun, H., Shi, Y., & Shi, W. (2021). Well-designed three-dimensional hierarchical hollow tubular g-C_3N_4/$ZnIn_2S_4$ nanosheets heterostructure for achieving efficient visible-light photocatalytic hydrogen evolution. *Journal of Colloid and Interface Science, 607*, 1391–1401.
33. Wang, L., Zhang, W., Su, Y., Liu, Z., & Du, C. (2021). Halloysite derived 1D mesoporous tubular g-C_3N_4: Synergy of template effect and associated carbon for boosting photocatalytic performance toward tetracycline removal. *Applied Clay Science, 213*, 106238.
34. Cui, D. H., Zheng, Y. F., & Song, X. C. (2017). A novel visible-light-driven photocatalyst Ag_2O/AgI with highly enhanced photocatalytic performances. *Journal of Alloys and Compounds, 701*, 163–169.
35. Xu, H., Cao, Y., Xie, J., Hu, J., Li, Y., & Jia, D. (2018). A construction of Ag-modified raspberry-like AgCl/Ag_2WO_4 with excellent visible-light photocatalytic property and stability. *Materials Research Bulletin, 102*, 342–352.
36. Dai, K., Lv, J., Lu, L., Liang, C., Geng, L., & Zhu, G. (2016). A facile fabrication of plasmonic g-C_3N_4/Ag_2WO_4/Ag ternary heterojunction visible-light photocatalyst. *Materials Chemistry and Physics, 177*, 529–537.
37. Zhang, W., Zhou, L., Shi, J., & Deng, H. (2017). Fabrication of novel visible-light-driven AgI/g-C_3N_4 composites with enhanced visible-light photocatalytic activity for diclofenac degradation. *Journal of Colloid and Interface Science, 496*, 167–176.
38. Zhang, H., Tang, G., Wan, X., Xu, J., & Tang, H. (2020). High-efficiency all-solid-state Z-scheme Ag_3PO_4/g-C_3N_4/$MoSe_2$ photocatalyst with boosted visible-light photocatalytic performance for antibiotic elimination. *Applied Surface Science, 530*, 147234.
39. Rajendran, R., Vignesh, S., Sasireka, A., Suganthi, S., Raj, V., Baskaran, P., Shkir, M., & AlFaify, S. (2021). Designing Ag_2O modified g-C_3N_4/TiO_2 ternary nanocomposites for photocatalytic

organic pollutants degradation performance under visible light: Synergistic mechanism insight. *Colloids and Surfaces A: Physicochemical and Engineering Aspects, 629*, 127472.
40. Mohamed, N. A., Ismail, A. F., Safaei, J., Johan, M. R., & Teridi, M. A. M. (2021). A novel photoanode based on Thorium oxide (ThO_2) incorporated with graphitic carbon nitride (g-C_3N_4) for photoelectrochemical water splitting. *Applied Surface Science, 569*, 151043.
41. Akulinkin, A., Bolgaru, K., & Reger, A. (2021). Facile synthesis of porous g-C_3N_4/β-SiAlON material with visible light photocatalytic activity. *Materials Letters, 305*, 130788.
42. Liu, J., Li, J., He, S., Sun, L., Yuan, X., & Xia, D. (2020). Heterogeneous catalytic ozonation of oxalic acid with an effective catalyst based on copper oxide modified g-C_3N_4. *Separation and Purification Technology, 234*, 116120.
43. Kokilavani, S., Syed, A., Thomas, A. M., Elgorban, A. M., Al-Rashed, S., Raju, L. L., & Khan, S. S. (2021). Integrating Ag_2WO_4 on VS_4 nanoplates with synergy of plasmonic photocatalysis and boosted visible-light harvesting and its antibacterial applications. *Journal of Alloys and Compounds, 865*, 158810.
44. Huang, H., Li, Y.-X., Wang, H.-L., & Jiang, W.-F. (2021). In situ fabrication of ultrathin-g-C_3N_4/AgI heterojunctions with improved catalytic performance for photodegrading rhodamine B solution. *Applied Surface Science, 538*, 148132.
45. Zhu, Y., Wan, T., Wen, X., Chu, D., & Jiang, Y. (2019). Tunable type I and II heterojunction of CoO_x nanoparticles confined in g-C_3N_4 nanotubes for photocatalytic hydrogen production. *Applied Catalysis B: Environmental, 244*, 814–822.
46. Nagajyothi, P. C., Pandurangan, M., Vattikuti, S. V. P., Tettey, C. O., Sreekanth, T. V. M., & Shim, J. (2017). Enhanced photocatalytic activity of Ag/g-C_3N_4 composite. *Separation and Purification Technology, 188*, 228–237.
47. Mousavi, M., & Habibi-Yangjeh, A. (2018). Magnetically recoverable highly efficient visible-light-active g-C_3N_4/Fe_3O_4/Ag_2WO_4/AgBr nanocomposites for photocatalytic degradations of environmental pollutants. *Advanced Powder Technology, 29*, 94–105.
48. Rajput, R. B., & Kale, R. B. (2021). Hydro/solvothermally synthesized visible light driven modified SnO_2 heterostructure as a photocatalyst for water remediation: A review. *Environmental Advances, 5*, 100081.
49. Jaleh, B., Nasrollahzadeh, M., Nasri, A., Eslamipanah, M., Moradi, A., & Nezafat, Z. (2021). Biopolymer-derived (nano) catalysts for hydrogen evolution via hydrolysis of hydrides and electrochemical and photocatalytic techniques: A review. *International Journal of Biological Macromolecules, 182*, 1056–1090.
50. Ji, X., Liu, X., Guo, Y., & Zhang, J. (2021). Developing visible light responsive Z-scheme BN-PDI photocatalysts with good degradation performance for antibiotics. *Chemical Engineering Journal, 425*, 131260.
51. Ma, B., Zhao, J., Ge, Z., Chen, Y., & Yuan, Z. (2020). 5 nm NiCoP nanoparticles coupled with gC_3N_4 as high-performance photocatalyst for hydrogen evolution. *Science China Materials, 63*, 258–266.
52. Ma, R., Zhang, S., Wen, T., Gu, P., Li, L., Zhao, G., Niu, F., Huang, Q., Tang, Z., & Wang, X. (2019). A critical review on visible-light-response CeO_2-based photocatalysts with enhanced photooxidation of organic pollutants. *Catalysis Today, 335*, 20–30.
53. Mousavi, M., Habibi-Yangjeh, A., & Rahim Pouran, S. (2018). Review on magnetically separable graphitic carbon nitride-based nanocomposites as promising visible-light-driven photocatalysts. *Journal of Materials Science: Materials in Electronics, 29*, 1719–1747.

Authors and Affiliations

Paria Hemmati-Eslamlu[1] · Aziz Habibi-Yangjeh[1] · Xuefei Xu[2] · Chundong Wang[2] · Alireza Khataee[3,4]

✉ Aziz Habibi-Yangjeh
ahabibi@uma.ac.ir

✉ Chundong Wang
apcdwang@hust.edu.cn

[1] Department of Chemistry, Faculty of Science, University of Mohaghegh Ardabili, Ardabil, Iran

[2] School of Optical and Electronic Information, Wuhan National Laboratory for Optoelectronics, Optics Valley Laboratory, Huazhong University of Science and Technology, Wuhan 430074, People's Republic of China

[3] Research Laboratory of Advanced Water and Wastewater Treatment Processes, Department of Applied Chemistry, Faculty of Chemistry, University of Tabriz, Tabriz, Iran

[4] Department of Environmental Engineering, Faculty of Engineering, Gebze Technical University, 41400 Gebze, Turkey